JACS
JOURNAL OF THE AMERICAN CHEMICAL SOCIETY
pubs.acs.org/JACS
Article

Unraveling the Kinetics of Hydride Formation and Decomposition at Pd−Au Bimetallic Interfaces: A Combined Spectroscopic and Computational Study

Prahlad K. Routh,[●] Xihan Liu,[●] Evgeniy Redekop,[●] Jin Soo Lim, Sebastian Prodinger, Jessi E. S. van der Hoeven, Joanna Aizenberg, Maarten Nachtegaal, Adam H. Clark, Philippe Sautet,* and Anatoly I. Frenkel*

Cite This: *J. Am. Chem. Soc.* 2025, 147, 11378−11389

Read Online

ACCESS | Metrics & More | Article Recommendations | Supporting Information

ABSTRACT: Supported Pd−Au bimetallic nanoparticles make up a promising class of catalysts used for hydrogenation and oxidation reactions. Recently, the role of dynamic restructuring of Pd regions at and near the nanoparticle surface in response to modulating gas (H_2 and O_2) concentrations was highlighted for controlling the surface Pd oxide stoichiometry. Here, we investigate the mechanism of formation and decomposition of Pd hydride (PdH_x) at and near the bimetallic nanoparticle surfaces, a key species for controlling the activity, selectivity, and stability of Pd catalysts in many hydrogenation reactions. We employ modulation excitation X-ray absorption spectroscopy (ME-XAS) to directly observe the time scale of PdH_x formation and decomposition on the surface of Pd−Au nanoparticles. Density functional theory (DFT) calculations provide additional insights into the stability and energetics of PdH_x formation under varying H fractions and Pd substructures. Our results reveal a complex interplay between Pd ensemble size, surface structure, and hydrogen environment in determining the kinetics and thermodynamics of PdH_x formation. By elucidating the mechanisms underlying surface PdH_x formation and decomposition, the rational design of dynamic catalysts with controlled Pd hydride stoichiometries can become possible.

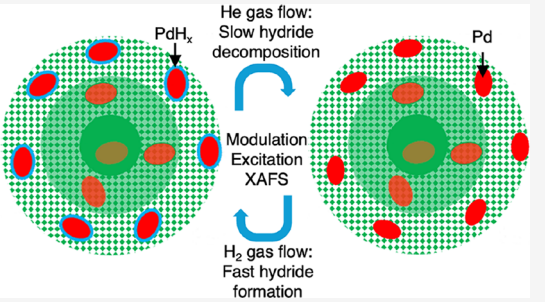

1. INTRODUCTION

Supported palladium and its alloy nanoparticles are widely used for catalysis, hydrogen separation, purification, and storage.[1] Recent studies have shown that the structure of the nearest environment of Pd atoms in different surface facets plays a key role in developing low-cost hydrogen carriers for practical fuel cell applications.[2] Pd ensemble sizes define the feasibility of H_2 activation and subsequent hydrogenation and dehydrogenation reactions. Hence, an optimal palladium structure, ranging from atomically dispersed to subnm and larger Pd clusters, is often needed for favorable adsorption and subsequent reactions.[3] In heterogeneous catalysis, Pd-based nanocatalysts catalyze the selective hydrogenation of alkynes for large-scale industrial applications.[4] The addition of a second metal, thereby forming alloys, enables a strategy to leverage geometric and electronic effects between the host metal and active catalytic centers to further improve selectivity and activity.[5,6] Recent efforts have also shown that the catalytic activity of bimetallic alloys can be tuned dynamically by pretreatment of Pd−Au catalysts, which results in changes in elemental distribution, ensemble size, and electronic structure at the surface, and can possibly enable metastable configurations that deviate from the thermodynamically most favorable configurations.[7−10]

Metallic Pd has a relatively high capacity to dissolve O, C, and H atoms and, depending on the gas environment, tends to form oxide, carbide, and hydride phases that may participate in catalytic reactions. In particular, in hydrogenation reactions, the formation of Pd hydride (PdH_x) is hypothesized to play a role in determining reaction activity and selectivity.[11−14] Palladium hydride (PdH_x) has been shown to exhibit a phase transition between a low-H content α−phase and high-H content β−phase, and more recently, a metastable hexagonal close-packed (hcp) structure at high H content in nanoscale particles has also been evidenced.[15] Pd hydride has been shown to be important for catalyzing hydrogenation reactions[16,17] and separation science with its application to membranes.[18,19] The H atoms in PdH_x can be located on the

Received: January 16, 2025
Revised: March 14, 2025
Accepted: March 17, 2025
Published: March 25, 2025

https://doi.org/10.1021/jacs.5c00842
J. Am. Chem. Soc. 2025, 147, 11378−11389

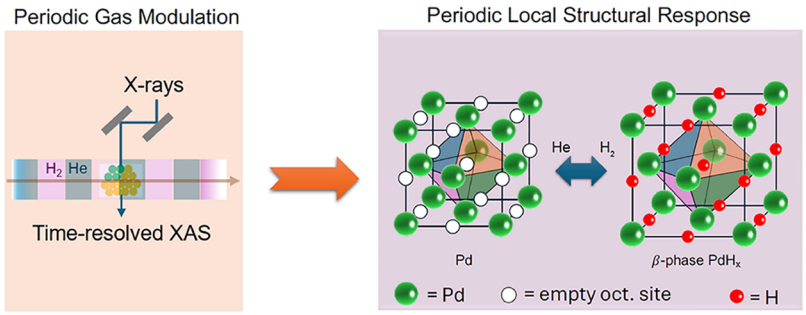

Figure 1. Schematic overview of time-resolved XAS experiments (left pane). ME-XAS experiment of Pd and 30%Pd−Au RCTs was conducted at 100 °C, while the pretreatment in He was carried out at 210 °C. Transformation between the Pd and PdH_x in the PdAu lattice (right pane).

surface, subsurface, and interstitial sites after the absorption and dissociation of H_2 on the surface of a Pd cluster or nanoparticle. Thermodynamic stability data[20] and in situ experimental observation of PdH_x in pure Pd nanoparticles (Pd NPs) have shown that H atoms introduce lattice distortions, and the stability of PdH_x is dependent on Pd nanoparticle size.[21] The kinetics of the formation of PdH_x in pure Pd and its bulk alloys are well-established,[22] but little is known about the kinetics of hydride formation in bimetallic Pd nanoalloys. This is largely due to the difficulty of characterizing subnanometric Pd domains and possible inhomogeneous Pd distribution in the alloy within larger bimetallic NPs with standard structural characterization methods such as XRD, XPS, and XAS. Pd and Au are highly miscible, but the intraparticle compositional and structural configuration can range from Au-core-Pd-shell[23,24] to Pd-core-Au-shell[25] structures, in addition to quasi-homogeneous mixing.[26,27] The surface distribution of Pd atoms in Pd−Au particles significantly influences the performance of the catalysts, e.g., isolated Pd sites are useful for CO oxidation[28] and higher H_2O_2 selectivity in H_2O_2 synthesis,[29] and Pd regions have been shown to have low energy barriers for the oxygen reduction reaction (ORR).[30]

The direct observation of the dynamic surface structures at the subnanometer level is experimentally challenging, and intermediate catalyst states are often not detected during steady-state experimental measurements. The heterogeneity of surface species remains a major research challenge.[31] Modulation excitation (ME) experiments, where the gas environment, temperature, or electric potential are periodically changed, have been shown to enhance the signal-to-noise ratio toward the detection of the surface species that actively participate in the (reversible) interaction. ME coupled with X-ray absorption spectroscopy (ME-XAS) also enables probing of intermediate states formed reversibly, present at low concentrations. In a recent study, we applied the ME-XAS approach to probe the dynamic restructuring of surface PdO_x, Pd, and Pd−Au species in bimetallic (Pd-in-Au) nanoparticles under modulating (H_2 and O_2) gas conditions.[32]

Herein, we examine the role of surface and subsurface Pd clusters in the dynamics of Pd hydride formation and decomposition, using the previously studied system of ca. 30 atomic % Pd−Au bimetallic nanoparticles (7.0 nm in diameter, with a standard deviation of 1.7 nm[32]) partially embedded in SiO_2 support (using a raspberry colloid templated (RCT) synthesis method).[32] The raspberry colloid synthesis approach is a multistep colloidal synthesis procedure for obtaining well-defined catalysts consisting of a macroporous metal oxide support (in this case, silica) with metallic nanoparticles (here: Pd−Au) residing at the pore walls.[32−34] A key feature of the system is that the nanoparticles are substantially embedded in the support, giving them high thermal stability and making the nanoparticles resistant to sintering at elevated temperatures and under catalytic conditions.

This Pd−Au system has been shown to possess a heterogeneous distribution of Pd atoms within the Au host, ranging from three-dimensional Pd-rich regions[32] to surface Pd_nAu (n = 1, 2, or 3) ensembles.[7] To capture details of the surface dynamics of the Pd−Au bimetallic nanoparticles, we designed herein an in situ approach and used periodic modulation of the gas environment between H_2 and He and quantified the local structure of Pd atoms in $Pd_{30}Au_{70}/SiO_2$ and Pd_{100}/SiO_2 nanoparticles by XAS using a fast acquisition rate of 1 Hz. For gas modulation, we used a total of 60 cycles, with each cycle consisting of 60 s of He and 60 s of 20% H_2 balanced with He. We hypothesize that periodic switching of gas pulses of He and H_2 will cause the periodic switching of the compositions of Pd regions, from metallic Pd to Pd hydride and back (Figure 1). This method enabled the observation of near-surface Pd hydride formation and decomposition time scales and estimated the fraction of Pd atoms at and near the surface of Pd regions participating in hydrogenation and dehydrogenation dynamics. To gain insight into the mechanism of the observed structural and kinetic changes in the Pd environment, we performed a systematic investigation of the stability of various Pd and PdH_x structures in Au as a function of a wide range of Pd and H concentrations by using density functional theory (DFT) calculations of Pd in model bimetallic surfaces. Using this approach, we accounted for the effects of hydrogen activation, diffusion, and absorption.

2. EXPERIMENTAL RESULTS AND DISCUSSION

2.1. Local Structure Determination of Pd and PdH_x in Pd−Au RCT Using Steady-State XAS. Prior work on PdH_x[12,35−37] has shown that using the empirical relationship (eq 1) between the Pd−Pd bond length change (ΔR), determined by steady-state EXAFS measurements, and y, the H/Pd ratio of palladium hydride, the latter can be obtained for Pd in Pd nanoparticles as well as Pd−Au bimetallic nanoparticles:

$$\frac{\Delta R}{R} = 0.066y - 0.0164y^2 \quad (1)$$

Table 1 lists the best-fit parameters obtained by the EXAFS analysis of spectra measured at RT under steady-state conditions in a He environment (the pre-MES and post-MES were measured before and after H_2/He modulation at 100 °C, respectively) and PdAuH in a H_2 environment, indicating an increase in Pd−Pd interatomic spacing from 2.77 to 2.80 Å, yielding $\Delta R/R$ = 0.011. The changes in the local coordination environment of Pd seem negligible (within experimental

https://doi.org/10.1021/jacs.5c00842
J. Am. Chem. Soc. 2025, 147, 11378−11389

Table 1. Ensemble-Averaged EXAFS Fitting Results under Steady-State Conditions at Room Temperature: Coordination Numbers, Distances, Their Mean Squared Disorder Values, and the Photoelectron Energy Origin Corrections[a]

	pre-MES (in He)	post-MES (in He)	PdAuH (in H_2)
N_{PdPd}	3.0(1.1)	3.6(1.3)	3.2(5)
N_{PdAu}	7.7(1.2)	7.6(1.4)	7.4(6)
R_{PdPd} (Å)	2.77(2)	2.77(2)	2.80(1)
R_{PdAu} (Å)	2.80(2)	2.80(1)	2.80(1)
σ^2_{PdPd} (Å^2)	0.008(3)	0.008(3)	0.004(1)
σ^2_{PdAu} (Å^2)	0.006(1)	0.006(1)	0.005(1)
ΔE_0 (eV)	3.2(6)	3.3(6)	3.2(3)

[a]The amplitude factor was obtained by the fit to Pd foil EXAFS and fixed to 0.8. Uncertainties in the last significant digits are given in parentheses. Further details are given in the SI (Section 3).

error) at room temperature. We note that the ratio of Pd−Pd and Pd−Au coordination numbers (Table 1) is greater than their relative fraction (1:3) in the alloy, consistent with segregation of Pd to Pd-rich regions, as expected. Using a crude estimate of the H/Pd ratio y = 0.17 (obtained after solving eq 1), two scenarios may be proposed. The first model, a homogeneous model, corresponds to H occupying, on average, 17% of all octahedral sites in all Pd regions with the nanoparticles. The second, a heterogeneous model, corresponds to a fraction of regions in the H occupancy that is 100%, coexisting with the metallic regions. Within the limitations of the ensemble-averaging nature of steady-state XAS, we cannot resolve these possibilities. The tie between them will be broken when ME-XAS is combined with theoretical modeling (vide infra).

In summary, XAS analysis of spectra collected under steady-state conditions shows that, from the ensemble-average perspective, the Pd−Au alloy does not undergo significant restructuring as a result of changing gas atmospheres. Furthermore, no significant change in Pd−Pd interatomic spacing is observed, before and after the modulation experiment. A clear increase in Pd−Pd interatomic spacing is observed, however, when the system is exposed to H_2 at room temperature, corresponding to saturated PdH_x in the 30% Pd−Au RCT system. Therefore, modulation excitation experiments, with enhanced sensitivity to the effects of H incorporation into Pd regions, may be more suitable for investigating these effects than steady-state experiments.

2.2. Time-Resolved XANES and EXAFS of Pd and Pd−Au RCTs. To characterize the Pd hydride formation kinetics, we utilized the multivariate curve resolution−alternating least-squares (MCR-ALS) method[38] to decompose the time-resolved XAS spectra of the core−shell Pd/PdH_x nanoparticle system. Prior to using this method, the variations between the spectra are first studied by principal component analysis that represents all of the time-resolved spectra using a small number (N) of (abstract) principal components. Later, an iterative process is used to deconvolve the data matrix into the N spectra of unique pseudospecies and their concentration profiles. The MCR-ALS analysis identified two pseudospecies in each experiment, which captured most of the signal variance. These species can be assigned to metallic Pd and the hydride PdH_x, respectively, based on the comparison of MCR-generated spectral components with reference/literature spectra for Pd and PdH_x (see Figure S1). Transient processes observed at the beginning of the H_2/He cycling were not included in the analyzed spectra by excluding the first 30 cycles for Pd and PdAu NPs. In agreement with previous reports,[39] the formation of PdH_x from monometallic Pd in H_2 flow was noticeably faster than its decomposition in He flow, as evident from Figure 2. We estimated the characteristic time scales of the PdH_x formation/decomposition as 6 and 12.2 s, respectively, by fitting a first-order exponential decay model into the corresponding signals.

As discussed above, steady-state XANES and EXAFS spectra of Pd−Au RCTs pretreated in H_2 at room temperature characterize the

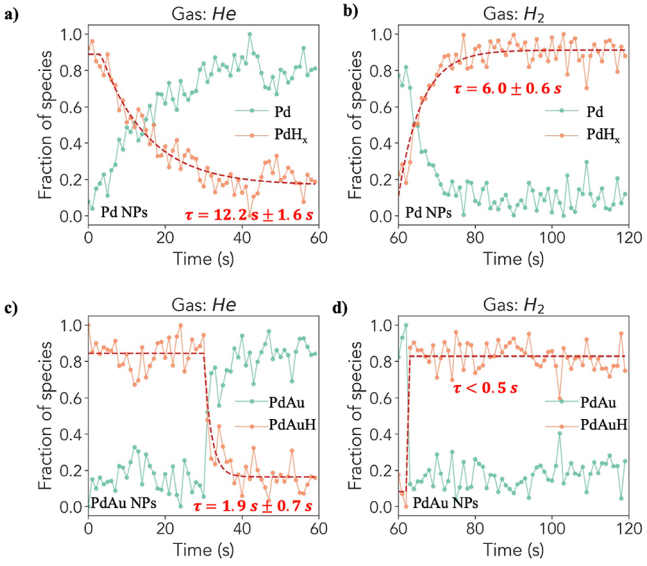

Figure 2. MCR-ALS analysis-based concentration profiles for two species using period-averaged spectra over 30 cycles for Pd nanoparticles pretreated in a He atmosphere at 210 °C. MCR-ALS analysis-based concentration profiles for two species using period-averaged spectra over 30 cycles in PdAu NPs pretreated in a He atmosphere at 1 atm. (a, c) He half-period of 60 s, while (b, d) H_2 half-period of 60 s. Dashed red lines show the exponential decay and rise profiles, which were used to obtain time-constants of Pd hydride decomposition (Pd: 12.2 s ± 1.6 s; PdAu: 1.9 s ± 0.7 s) and formation (Pd: 6.0 s ± 0.6 s; PdAu: < 0.5 s).

saturated hydrogenation state (PdAuH) of Pd−Au RCTs, with an ensemble-average content of PdH_x formation corresponding to a H/Pd ratio of 0.17. MCR-ALS-based time-resolved XANES spectra (Figure S1b), when compared with these steady-state conditions, highlight that Pd−Au RCTs do not undergo complete hydrogenation and dehydrogenation between two half-cycles. Data in Figure 2 reveal important differences in the kinetics of PdH_x formation and decomposition between the samples. While for monometallic Pd, the decomposition of PdH_x begins immediately after the flow switch from H_2 to He, a pronounced induction period of about 30 s is observed for bimetallic Pd−Au before PdH_x begins to decompose after the switch. Additionally, it can be observed that the rates of Pd-PdH_x interconversion are greater for Pd−Au than for Pd during both the formation of PdH_x (characteristic time of less than 0.5 s, likely mass-transfer-limited) and its decomposition after the induction period (characteristic time of 1.9 s).

2.3. Differential XANES and EXAFS Analyses. Further insight about the reversibly forming surface and near-surface species can be obtained via demodulation of XANES and EXAFS spectra, which delineates the signal between spectators and active species.[32,40−43] Figure 3a shows the demodulated EXAFS spectra obtained via phase-sensitive detection (PSD), representing the reversible changes in the Pd−Au RCTs in the phase domain. Demodulated EXAFS, in principle, encodes average first-order kinetics information, which can be compared between species and/or samples, e.g., species with faster kinetics achieve a maximum at higher phase angles.[41] However, in the presence of a pronounced induction period and asymmetric kinetics of hydride formation and decomposition, as seen in Figure 2, a direct interpretation of time domain spectra would be more helpful. Hence, a reconstruction of differential EXAFS via time domain is obtained after applying a denoising process explained in ref 32. In brief, the time-energy absorption coefficient 2D data matrix was processed by an iterative algorithm to remove the uncorrelated noise in the time domain for each energy point. Figure 3c shows the thus obtained differential EXAFS signal ($\Delta\mu = \mu(t) - \mu_{avg}$) after subtracting the time-average EXAFS signal from all individual EXAFS spectra in the full modulation period. Such subtraction

https://doi.org/10.1021/jacs.5c00842
J. Am. Chem. Soc. 2025, 147, 11378−11389

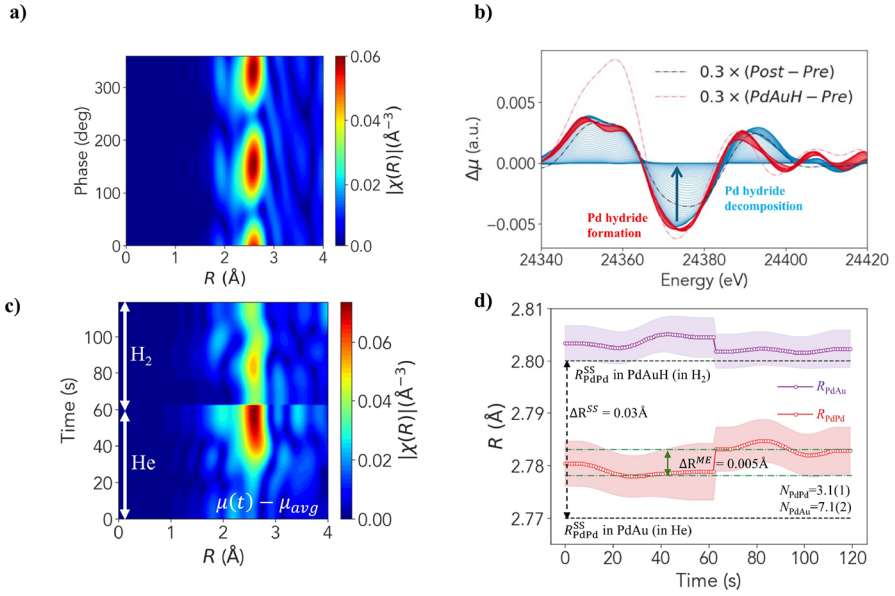

Figure 3. Phase domain (a) and denoised time domain (c) differential spectra of 30% Pd−Au RCT nanoparticles. XANES and EXAFS spectra are period-averaged over 30 cycles (C30−C60) and followed by denoising within each half pulse. (b) Time-dependent differential XANES is calculated by subtracting the last spectrum in the He half-period from the period-averaged data set. Red- and blue-colored spectra correspond to H_2 and He half-periods, respectively. The dashed lines denote the steady-state differential XANES with respect to PdAu in He at room temperature prior to modulation: full PdAu hydride (PdAuH) at room temperature in H_2 (shown in red) and PdAu in He at room temperature after modulation (shown in black). (d) Time-dependent EXAFS results: interatomic spacing between Pd−Pd (red) and Pd−Au (purple). The switch between He and H_2 occurred in 60 s. Black (dashes) lines show the interatomic spacing, R^{SS}, under steady-state conditions, indicating the partial nature of hydride formation and decomposition under modulated conditions. Green (dash-dots) lines show the limits of variation of R^{ME}, the interatomic spacing between Pd−Pd, during the modulations.

isolates the signal from "spectator" species whose spectral contribution does not change reversibly during the gas modulation.

Bugaev et al. have shown previously that spectral features in Pd K-edge XANES are also correlated with PdH_x formation.[44] Figure 3b shows the time-dependent evolution of these features as differential XANES signal with respect to the last time-step of PdAu in He half-cycle data during the modulation. A relative comparison of the spectral changes in post-MES vs pre-MES (for comparison, we also used the relative changes between the PdAuH and pre-MES as well) data, and the maximum variation in the MES data shows that, approximately, up to 30% of all Pd atoms participated in Pd hydride formation/decomposition during the modulation. These denoised EXAFS data (Figures S2 and S4) are further analyzed by traditional EXAFS analysis (Figures S3 and S4). The fitting variables were the same as those for the steady-state analysis. All the time-dependent data were analyzed concurrently by applying the following global constraints: the same value of ΔE_0 was varied for all 120 spectra (obtained to be 4.20 ± 0.05 eV), and the Pd−Pd and Pd−Au coordination numbers were constrained to be constant as well (Figure 3d). The H/Pd ratio was obtained to change between 8 and 11% (after applying eq 1 to the data shown in Figure 3d, where the meaning of ΔR is the difference between the Pd−Pd distance in the ME-EXAFS experiment and the steady-state values). Hence, both differential XANES and EXAFS data show that the cyclic formation and decomposition are only partial. A closer examination of the first cycle in MES, which shows only formation of Pd hydride and no decomposition, indicates fast kinetics of hydride formation (Figure S5), similar to the trend shown in Figure 3b. However, the relative scale of differential XANES (Figure 3b vs Figure S5) indicates that Pd−Au undergoes near complete hydride formation in the first half-cycle of H_2, and subsequent cycles undergo only partial hydrogenation and dehydrogenation.

Previous characterization of the Pd−Au RCT catalysts identified the presence of large Pd-rich regions within the bulk Au.[7,32,35,45] Our structural model arising from EXAFS analysis of time-resolved ME-XAS data also indicates that the Pd atoms are on-average coordinated with ∼3 other Pd atoms. With respect to the kinetics of Pd hydride formation and decomposition, our observations indicate that while there are similarities between the Pd−Au and Pd NPs, there are also key differences. The similarity is that in both types of catalysts, Pd hydride formation occurs much faster than decomposition. The difference is that in Pd−Au alloys versus Pd NPs, there is a clear delay of Pd hydride decomposition in the He pulse. Such a delay indicates the presence of distinctly different energy barriers at the onsets of hydride formation and decomposition (Figure 2). In addition, in the demodulated and differential ME-EXAFS spectra, the data (Figure 3a−c) deviated from the spectral differences of the two opposite states measured under steady-state conditions, with and without hydrogen. As shown in ref 32, the demodulated data (for the O_2 and H_2 gas pulses) could be represented as the difference between the two end states (PdO and Pd metal). Modulation conditions of He and H_2 gas pulses in the current study did not lead to detectable changes in the coordination environment of Pd. However, the Pd−Pd interatomic spacing changes (Figure 3d), a proxy for PdH_x formation, showed intriguing results, where partial but reversible formation and decomposition with noticeable time delays in the H_2−He pulse experiments, indicating an energy barrier at the onset of gas pulses.

We note that the interpretation of trends in the transient XAS data presented herein crucially relies on the rigorous evaluation of the characteristic time scales relevant for the chemical transformations and transport phenomena within the sample. As demonstrated previously,[32] under the operating conditions in the same setup as the one used in this work, the characteristic time scale of convective gas transport through the entire sample bed is on the order of 0.001 s, i.e., much smaller than the time scale of the changes observed in Figure 2. We note also that the XAS signal observed for monometallic Pd begins to change in response to the change of gas composition immediately after the switch in both the H_2-to-He and He-to-H_2 directions (Figure 2a,b). Notably, the signal evolves at a rate that is much slower (on the order of tens of seconds) than the imposed perturbation (0.005 s) or the characteristic (plug flow reactor) convective transport through the bed (0.001 s, vide supra), with PdH_x

https://doi.org/10.1021/jacs.5c00842
J. Am. Chem. Soc. 2025, 147, 11378−11389

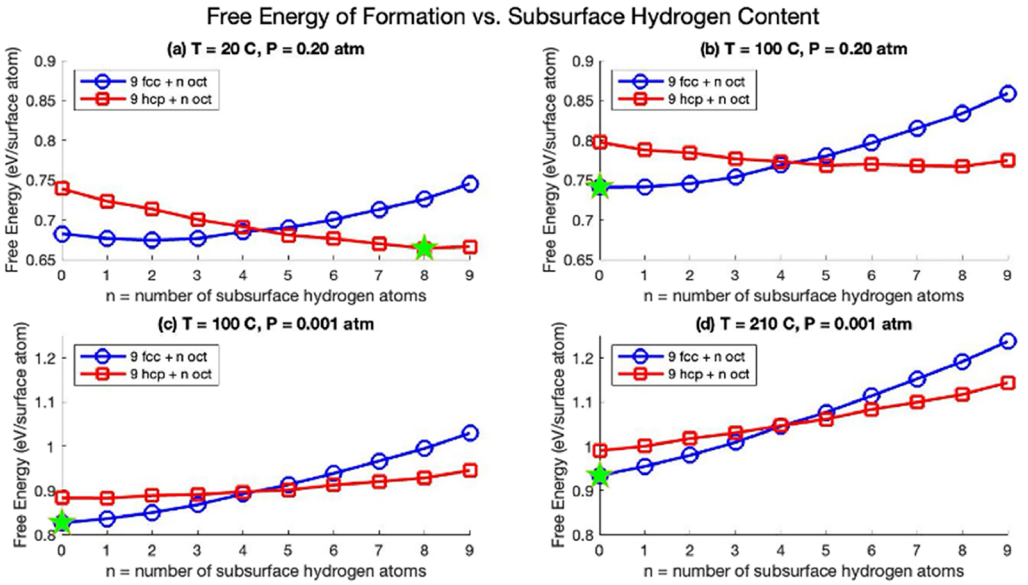

Figure 4. Free energies of formation as a function of subsurface hydrogen content for the bilayer structures under different experimental conditions from DFT calculations, (a) T = 20 °C, $P(H_2)$ = 0.20 atm; (b) T = 100 °C, $P(H_2)$ = 0.20 atm; (c) T = 100 °C, $P(H_2)$ = 0.001 atm; and (d) T = 210 °C, $P(H_2)$ = 0.001 atm. All of the points include the vibrational entropy and zero-point energy. In all selected conditions, the surface is completely populated with H adsorbates, which preferentially occupy the surface fcc (blue circles) or hcp sites (red circles) at, respectively, low or high subsurface H content. The most stable structure under each experimental condition is starred in green.

formation in a H_2 atmosphere being significantly faster than PdH_x decomposition in He.

The XAS signal observed for the bimetallic PdAu samples behaves drastically differently from that of the monometallic counterpart. First, the kinetics of PdH_x formation/decomposition is much faster (on the order of a few seconds) for the bimetallic sample, which can be seen very clearly by comparing responses in Figure 2b,d. The kinetics of PdH_x formation in PdAu (Figure 2d) is the fastest signal observed in our data set and, as such, delineates the lower boundary of the mass-transport rate at the reactor scale. In other words, even if this signal reflects mass transport rather than chemistry, all other signals that are slower (Figure 2a–c) must definitely reflect the kinetics of chemical transformations.

The second (qualitative) difference between Pd and PdAu samples is the approximately 30 s induction period observed in Figure 2c between the start of the He half-period (H_2-to-He switch) and the start of PdH_x decomposition. In view of the aforementioned assertions regarding the rate of mass transport in the reactor, this induction period can be confidently interpreted as a purely chemical phenomenon.

In summary, experimental data and analysis results pose the following questions that, we hypothesize, can be answered in terms of the local structure and composition of Pd–Au and PdH_x species: (1) Why were the changes observed during the H_2–He modulation partial and reversible? (2) Why was there a delay in the hydrogen desorption portion of the modulation period (the hydrogen adsorption appeared to be virtually instantaneous)? (3) Why were the rates of formation and decomposition of PdH_x so different?

3. THEORETICAL STUDY

For an in-depth understanding of the stability of Pd hydride species and hydrogen diffusion pathways responsible for the observed experimental barriers (for the reaction kinetics and for the presence of an induction period), we further conducted an ab initio study of various Pd hydride structures and activation mechanisms by DFT calculations. Previous work on surface and subsurface hydrogen adsorption showed that surface H_2 activation is generally exothermic, and subsurface hydride formation is typically endothermic, with Pd being the only exception.[46] Weaker binding and lower diffusion barriers into the subsurface in near-surface alloys (NSA) compared to the monometallic counterparts have been reported.[46] Hence, a stability assessment of various hydride structures under the modulated experimental conditions was carried out to identify potential stable and metastable candidate structures. A detailed scheme to evaluate the formation energy of various structures is shown in Figure S6. Previous DFT studies have also suggested that the surface hydrogen diffusion barriers were quite low for all 23 transition-metal surfaces that were investigated, with the barrier ranging from 0.04 to 0.28 eV.[47] A more detailed study of hydrogen diffusion pathways was conducted hereby to explain the observed hydride formation and decomposition time scales (see Section 3.2).

3.1. Stability Assessment of Hydride Structures. A diverse range of structures with various ensembles of Pd on Au was examined using DFT calculations, sampling these structures under different hydrogen coverages and calculating their normalized formation energy (see Figures S7 and S8). These calculations show that stable formation of hydride species under H_2 pressure reaction conditions requires extended Pd regions modeled as Pd layers on gold (Figure S9). Here, we explore these layer models of Pd-rich regions observed in the experiments in detail.

We will first examine the hydride structures in the bilayer structure that includes two layers of Pd on two layers of Au, therefore with a total of four layers in the (3 × 3) periodic slab. The surface presents a (111) termination. From the initial hydrogen population, where we introduced up to nine hydrogen atoms into the 3 × 3 bilayer Pd slab into the surface or the subsurface layer, we observed that the surface hydrogen atoms had a better stabilization effect than the subsurface hydrogen atoms. The stabilization effect was maximized with nine surface atoms, reaching a 1:1 H-to-Pd ratio for the surface atomic layer, with all H atoms at fcc sites. Also, we were not able to find any metastable structures for the subsurface population at low hydrogen coverages (0 to 2/3

https://doi.org/10.1021/jacs.5c00842
J. Am. Chem. Soc. 2025, 147, 11378–11389

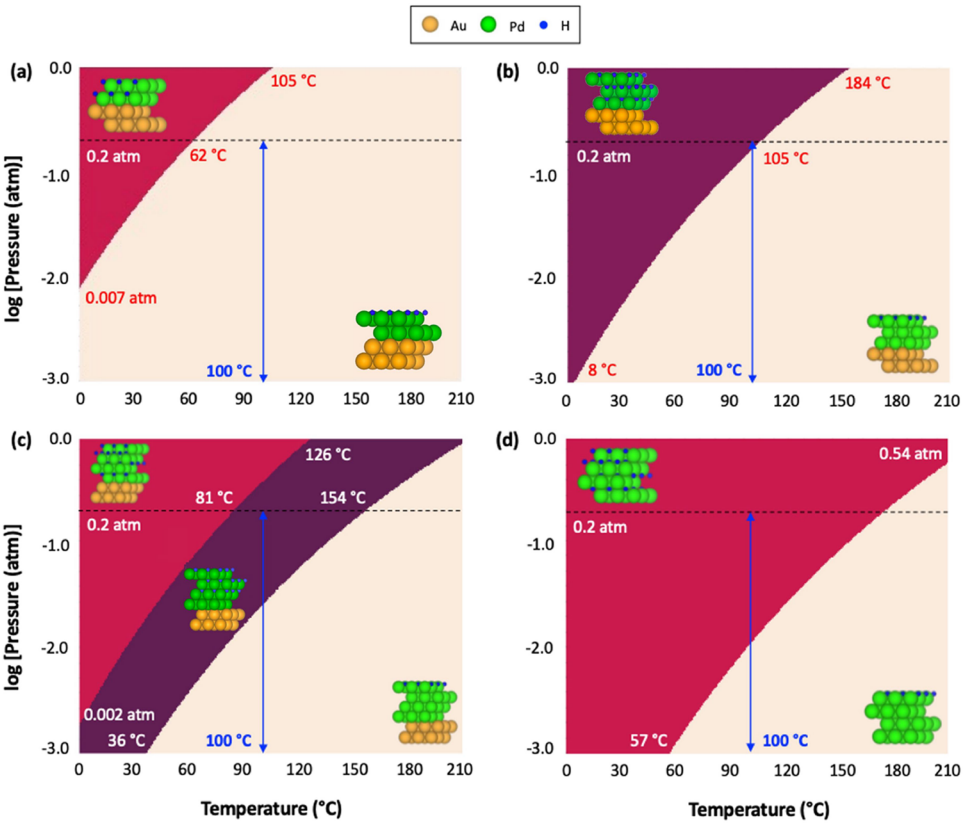

Figure 5. Stability diagram computed from ab initio thermodynamics for: (a) Pd bilayer, (b) Pd trilayer, (c) Pd tetralayer, and (d) pure Pd with varying surface/subsurface H concentrations. For simplicity, only structures with the maximum number of H atoms in each layer are considered. Each layer can have a maximum of nine H atoms in the 3 × 3 unit cell. The blue arrow indicates the experimental modulation conditions at 100 °C.

ML). Even at higher hydrogen coverages (2/3 to 1 ML), the subsurface-populated structures were higher in energy than the surface-populated counterparts (see Figure S7). Therefore, the surface sites are clearly populated first, and subsurface occupation only starts when the surface coverage is 1 ML.

We kept the surface layer of our 3 × 3 unit cell fully covered by a total of nine hydrogen atoms and began to introduce additional hydrogen atoms in the subsurface layer. For the surface hydrogen atoms, we considered both fcc and hcp hollow sites. For the subsurface hydrogen atoms, we only took the octahedral sites (oct) into account, since the octahedral hydrogen atoms were always more stable than the hydrogen atoms at the tetrahedral sites (tet) for both fcc and hcp positions of the H adlayer. Our results were in good agreement with previous work.[46,48] Additionally, we found the vibrational entropy and zero-point energy corrections pivotal in the cases where the hydrogen coverages were high, as shown in the Supporting Information. This finding was also confirmed by Nazarov et al.[48] Without these two factors, we inferred that it was barely likely to determine the most stable structures accurately from our calculations. Hence, the free energy calculations for structures with high hydrogen coverages included vibrational entropy and zero-point energy corrections.

The normalized free energies were computed under four different experimental conditions, as shown in Figure 4. At room temperature and 0.2 bar of H_2, the subsurface layer is almost fully occupied (8/9 ML coverage), and the most favorable configuration corresponds to surface H atoms in the hcp position, hence in a different position compared to the case where the subsurface is vacant. It should be noted that populating the second subsurface layer is not favorable, since the octahedral sites in this layer are formed by 3 Pd and 3 Au, and the binding energy of H is unstable. At high temperature (210 °C) and low H_2 pressure (taken as 0.001 bar), no subsurface site is occupied, and only the surface remains completely full (H atoms in fcc sites). This suggests that modulation of the H content could be achieved by desorption of the subsurface H atoms, keeping the surface occupied. However, for the two-Pd-layer model, under the conditions of experimental modulation (T = 100 °C, P varied from 0.2 to 0.001 bar, an estimate of the H_2 partial pressure under He flow, Figure 4b,c) no modulation of the H concentration is seen, and only the surface sites are occupied. We also developed a 2D stability diagram for the bilayer model to help visualize the most stable structures under different temperature and pressure conditions (see Figure S10).

We performed a similar analysis for other Pd structures, namely, the Pd trilayer structure, the Pd tetralayer structure, and the pure Pd(111) structure, and the side view of each structure and its stability diagram are shown in Figure 5. In this analysis, we did not consider the partially H-covered case for each Pd layer. Only the fully vacant and fully occupied H layers were included in the diagram. As we increased the number of layers of Pd, the shaded region, representing the stability region of the hydride structures, also broadened. We also observed that all of the structures would undergo modulation (as shown by the blue arrow in Figure 5), except for the bilayer structure, as discussed earlier. This could also robustly explain the experimental observations that the modulation was partial and reversible. In the modulation, the gas environment

https://doi.org/10.1021/jacs.5c00842
J. Am. Chem. Soc. 2025, 147, 11378−11389

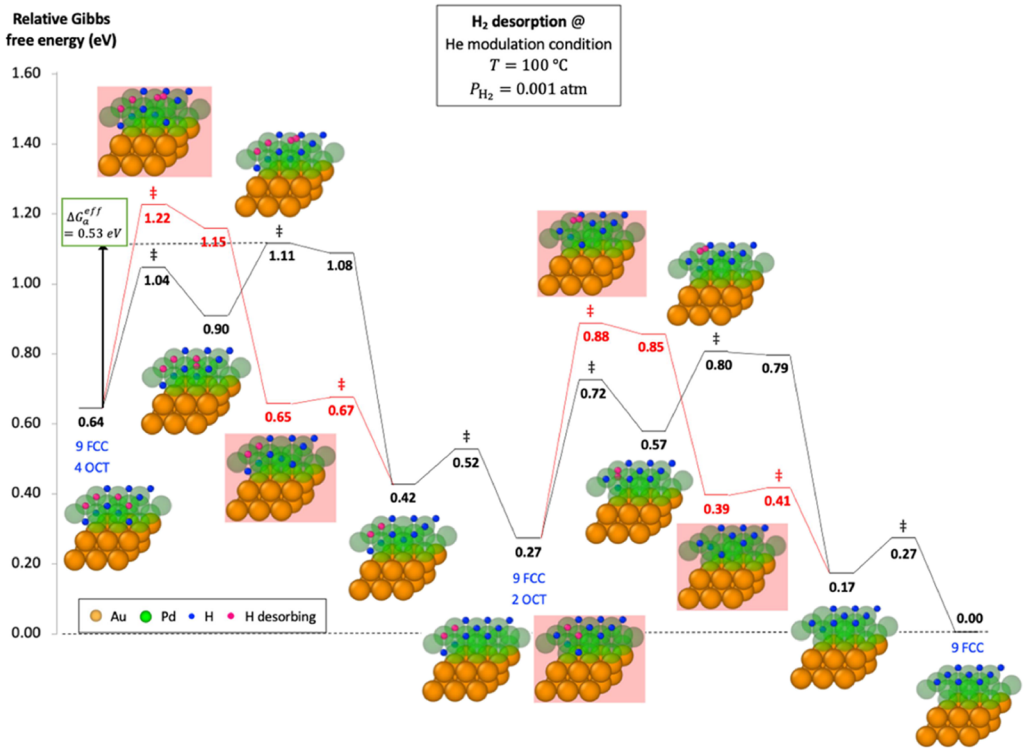

Figure 6. DFT-computed Gibbs free energy profile for the hydride decomposition process. The black and red lines represent two mechanisms under the He modulation condition where T = 100 °C and P_{H2} = 0.001 atm.

switched repeatedly between He and H_2, and hydride species exhibited very different stabilities under the two conditions. Consequently, the hydride species during the modulation changed back and forth, as the conditions switched. Moreover, our DFT calculations showed that the change in the hydride species only took place in the subsurface, and the surface remained fully covered throughout the modulation. Finally, the modulation in the subsurface hydride species requires significant Pd domains, which represent only a fraction of the available Pd in the system.

3.2. Hydride Formation and Decomposition. Removing or adding subsurface H atoms and keeping the surface site fully occupied are challenging from a mechanistic aspect since the desorption of subsurface H requires their migration via the surface, where desorption can occur. To better understand this aspect, we performed a mechanistic modeling of the hydride formation and decomposition processes using DFT calculations. The modeling was performed on the bilayer model, and thicker models were not considered due to the high computational cost. In the decomposition process, we started with the 3 × 3 surface fully covered (nine hydrogen atoms in fcc positions) plus four H atoms in subsurface octahedral sites. We continuously removed the hydrogen atoms in the subsurface layer until only the surface was occupied (9 H in the fcc sites). Two different plausible mechanisms were proposed under the He modulation conditions (T = 100 °C and $P(H_2)$ = 0.001 atm), as shown in Figure 6. In the pathway shown with red lines, two surface hydrogen atoms (labeled in red) are first combined, forming a surface vacancy and one H_2 adsorbate. The hydrogen molecule is then desorbed, forming a second vacancy, and two subsurface hydrogen atoms migrate to the surface layer to fill up the two vacancies. The procedure is repeated to remove the two remaining subsurface H atoms. In contrast, in the pathway shown with black lines, one surface hydrogen atom (labeled in red) migrates to a nearby hcp site, opening a site for one subsurface H atom to migrate to the surface. This creates a metastable surface with one hydrogen atom beyond full coverage (a 9+1 H configuration). A hydrogen molecule is then formed and desorbed from the surface, and another hydrogen atom migrates to the surface to fill the new vacancy. Another two hydrogen atoms are removed in a similar fashion before reaching the structure with 9 H on the surface and no subsurface H. The black pathway has a lower overall free energy barrier (0.53 eV). The pathway of the reverse process under the H_2 modulation conditions (T = 100 °C and $P(H_2)$ = 0.2 atm) is shown in Figure S11. Furthermore, we developed pathways for hydrogen diffusion and computed the energy profile for pure Pd and Pd-Au alloy using different lattices (Figures S12–S15). We observed that the lattice parameter could impact the energy barrier for diffusion, and that the penetration of hydrogen from the Pd layer to the Au layer was thermodynamically unfavorable.

We explain the delay for the desorption process by the necessity of removing some surface hydrogen to enable the subsurface hydrogen to migrate and desorb. As aforementioned, after the H_2 pulse in the modulation, the surface is fully covered, and there is no free channel for subsurface hydrogen content to desorb. While the thermodynamics in the He pulse allows subsurface H to desorb, this must be preceded by the desorption of more strongly bound surface H atoms, or by the formation of a metastable structure with one H atom displaced, to enable a subsurface H to desorb. This creates an extra barrier for the process. The Pd–Au alloy has a larger lattice constant, resulting in a larger Pd–Pd distance for the Pd-rich regions of interest here. This results in stronger H adsorption on the surface, resulting in a larger barrier to create the surface vacancy, and therefore a longer induction period. The delay in H desorption observed in the experiment could, therefore, be

https://doi.org/10.1021/jacs.5c00842
J. Am. Chem. Soc. 2025, 147, 11378–11389

explained by a "cork" effect created by the strongly bound surface H atoms, preventing the desorption of subsurface H atoms. For the creation of the hydride (adsorption process under H_2) H atoms at the fully occupied surface can readily penetrate in the subsurface, resulting in a lower barrier and a faster process.

4. UNIFYING EXPERIMENTAL AND THEORETICAL RESULTS

The insights gained by correlating the steady-state and ME-XAS measurements with theoretical modeling enabled us with a much more detailed picture of Pd-in-Au catalysts compared to our previous studies.[7,35,49] Our electron microscopy analysis[7,34] utilized the high-angle annular dark field (HAADF)−scanning transmission electron microscopy (STEM) imaging and elemental mapping to observe the segregation of Pd regions within the Au host (Figure S16), in agreement with previous studies.[32,35] This observation confirms the conclusions from the steady-state EXAFS data (Figure 7a,b). In the current work, by combining the insights from ME-XAS experiments and theoretical modeling, we resolve more details about the Pd segregation, separating them into three groups: Pd regions near the Au surface that change dynamically between metal and hydride (we call them "active"); metallic Pd regions in the Au core; and Pd hydride regions in the Au shell between the core and the surface (both of such Pd regions are "spectators" because they do not restructure in response to the H_2−He gas modulation (Figure 7c). In order to describe the state of the hydride in the outer region, responding to the gas modulation, we employ the observation that the difference between the ME XANES spectra between the two extremes (Figure 3b) can be compared to the difference between the two steady-state spectra and used to quantify the relative fraction of Pd atoms that undergo restructuring, which does not exceed approximately, 0.3 (Figure 3b), similar to the analogous scaling procedure performed previously.[32] Therefore, the changes in the average interatomic distance (Figure 3d), which can be approximated as the weighted fraction of changes for "active" and "spectator" species, can be used to estimate the Pd−Pd distance in the Pd hydride. Hence, the interatomic spacing changes in local Pd regions (active species) should be approximately 1/0.3 times greater than the increase of 0.015 Å shown for the PdH_x region in Figure 3d. As a result, $\Delta R_{active} = \langle \Delta R \rangle / x$, where x is the fraction of "active" species. Therefore, the R_{PdHx} can be estimated as 2.77 Å + 0.013/0.3 Å ≈ 2.81 Å, which is in a very good agreement with the literature for the Pd−Pd distance with stoichiometric Pd hydride,[36] and, hence, characterizing the H occupancy in the outer region as nearly 100%.

Under the modulation excitation conditions, the changes occur between the two states of the particles (corresponding to the He and H_2 pulses) involving only outer Pd atoms with the fraction of f_1. The remaining Pd atoms, partitioned into two regions (the hydride, in the interior shell, with the fraction of f_2, and metallic, in the core, with the fraction of $f_M = 1 - f_1 - f_2$), are unaffected by the modulating atmospheres. This conclusion is based on the evidence that the Pd−Pd distance under the He pulse during the ME experiment is greater than the corresponding distance under the steady-state experiment (Figure 3d); hence, some hydride phase is present during the He pulse in the ME experiment, while under the steady state, no such phase should be expected in the He regime. The average Pd−Pd distances measured by EXAFS in the He pulse and in H_2 pulse are related to each other via eqs 2 and 3:

$$R_{He}^{ME} = (1 - f_1 - f_2)R_M + f_2 R_{PdH_x} + f_1 R_M \quad (2)$$

$$R_{H_2}^{ME} = (1 - f_1 - f_2)R_M + f_2 R_{PdH_x} + f_1 R_{PdH_x} \quad (3)$$

Therefore,

$$f_1 = \frac{R_{H_2}^{ME} - R_{He}^{ME}}{R_{PdH_x} - R_M} = \frac{\Delta R^{ME}}{R_{PdH_x} - R_M} \quad (4)$$

Under steady-state conditions, the average Pd−Pd distances under He and H_2 atmospheres are related to each other as follows:

$$R_{He}^{SS} = R_M$$

$$R_{H_2}^{SS} = (1 - f_1 - f_2)R_M + f_2 R_{PdH_x} + f_1 R_{PdH_x}$$

Therefore,

$$f_1 + f_2 = \frac{R_{H_2}^{SS} - R_{He}^{SS}}{R_{PdH_x} - R_M} = \frac{\Delta R^{SS}}{R_{PdH_x} - R_M} \quad (5)$$

Combining eqs 4 and 5 yields

$$f_2 = \frac{\Delta R^{SS} - \Delta R^{ME}}{R_{PdH_x} - R_M} \quad (6)$$

Using the results for ΔR^{SS} = 0.03 Å (Figure 3d), ΔR^{ME} = 0.005 Å (Figure 3d), $R_M = R_{He}^{SS}$ = 2.77 Å (Figure 3d), and, assuming the full H occupancy in the hydride regions, as demonstrated above, R_{PdHx} = 2.81 Å, we estimate the values for f_1, f_2, and f_M as 10, 58, and 32%, respectively. Although this estimate is based on several approximations, the chief of them—the narrow size and compositional distributions of Pd−Au nanoparticles—have been validated in previous works.[7,32]

As a result, by combining the steady-state and ME experiments, we could resolve the heterogeneous distributions of Pd atoms in the Au nanoparticle, which is unavailable to either one of the experimental modes. Furthermore, theory played a critical role in arriving at this model (Figure 7). Indeed, the presence of surface H adsorbates blocks the desorption paths of H from the interior Pd regions, stabilizing them during the He pulses. Experimentally, this stabilization of H is evident via the elongation of the R_{He}^{ME} vs R_{He}^{SS} by ca. 0.01 Å (Figure 2d).

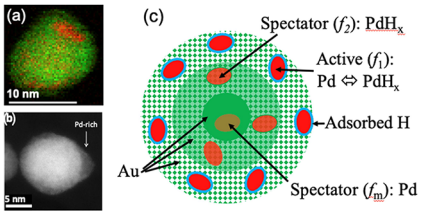

Figure 7. HAADF-STEM images of Pd distribution in previously investigated Pd−Au RCT alloys showing segregation of Pd within Au (a: ref 35. Copyright (2019) Wiley. Used with permission from Guan et al., New Role of Pd Hydride as a Sensor of Surface Pd Distributions in Pd−Au Catalysts. *ChemCatChem* **2020**, *12*, *717*−*721*, and b: ref 32, reproduced with permission from Springer Nature). Schematic of the structural changes in Pd species within the Pd−Au alloys (c in this work). Red zones represent the Pd-rich regions that, in the outer shell, are active (absorb/desorb hydrogen) during H_2−He modulation.

5. CONCLUSIONS

In this work, we combined experimental techniques and theoretical tools to investigate the stability of hydride species and the kinetics of hydride formation in Pd-Au alloys and pure Pd nanoparticles. In the modulation under He and H_2 gas conditions, we observed that the hydride formation process was partial and reversible. The DFT calculations indicated that the stability of hydride species under the two gas environments varied, and each time the gas environment changed, the hydride species changed from one to the other, making the process reversible. Moreover, only the subsurface hydrogen was modified during the modulation, and the surface remained fully covered, making the process partial.

https://doi.org/10.1021/jacs.5c00842
J. Am. Chem. Soc. 2025, 147, 11378−11389

In the experiments, we also found that for both catalysts, Pd and Pd−Au, the decomposition occurred more slowly than the formation process. Also, there was a noticeable delay in the decomposition process in the Pd−Au RCTs, but such a delay was not observed in pure Pd. Our DFT results demonstrated an obvious cork effect in which the stable hydrogen surface layer impeded the desorption of the less stable subsurface hydrogen, explaining the slower decomposition of the hydride under He modulation periods. There was no free channel for subsurface hydrogen to desorb as the surface is fully occupied, and the desorption of subsurface hydrogen always required the removal of some surface hydrogen, which was not thermodynamically favorable. On the other hand, in the adsorption process, the surface hydrogen could easily migrate downward to the subsurface as the subsurface was completely or partially available. Also, in the alloy, the lattice was stretched by the substantial Au constituent, and the hydrogen adsorption energy was larger, making the opposite process, namely, desorption, more difficult. Therefore, such a delay appeared only in the alloy and not in pure Pd. Intriguingly, we noticed that the rate of hydride formation in the Pd-Au alloy was faster than that in pure Pd. We inferred that hydrogen adsorption was controlled by hydrogen diffusion. The diffusion in pure Pd was three-dimensional, whereas it was considered two-dimensional in the alloy as the hydrogen atoms were only enclosed within the Pd region, where hydrogen adsorption was much stronger.

In summary, our integrated experimental and theoretical investigations reveal the complex interplay of stability, kinetics, and structural factors governing hydride formation and decomposition in Pd and Pd-Au nanoparticles, advancing our understanding of hydrogen dynamics in catalytic systems.

6. EXPERIMENTAL METHODS

The samples were synthesized and characterized as explained in ref 32. HAADF-STEM and STEM-EDX analyses were performed to study the morphology, size, and metal distribution of the 30% Pd−Au RCT catalysts using a ThermoFisher Spectra 300 electron microscope operated in STEM mode at 300 kV. The sample was pretreated in 20% H_2 in He at 400 °C for 40 min (ramp +10 °C/min to 400 °C) and cooled in He. Thereafter, it was dispersed in ethanol and drop-casted onto a carbon-coated TEM grid.

The time-resolved quick-scanning X-ray absorption spectroscopy measurements at the Pd K-edge absorption were taken at the SuperXAS beamline of the Swiss Light Source, Paul Scherrer Institute, Switzerland. The setup of the ME-XAS experiments was described in detail in ref 50. To obtain high-quality spectra, XAS data were collected in the total-fluorescence-yield mode with a time resolution of 0.5 s per scan using a PIPS detector. However, processed data were used with a 1s time interval. XAS in Pd foil, placed between the two ionization chambers located downstream of the reactor, was measured as a reference to calibrate the energy scale. The reactor effluent was monitored during the experiments with an online Pfeiffer quadrupole mass spectrometer connected to the outlet of the capillary reactor. In order to modulate the gases, two fast-acting three-way valves (Parker Series 9) were synchronized with a single TTL signal, actuating simultaneously directly one flow to the reactor and another flow to the exhaust vent. Our setup imposes the switch in the inlet H_2 (or He) concentration with a nominal actuation time of 0.005 s. Using this setup, modulation excitation with a period of 120 s with a concentration modulation of the gas atmosphere was performed using a periodic pulse of 60 s 20% H_2 (in He) and pure He gas pulses. The samples were pretreated before the x-ray absorption spectroscopy measurements according to the protocol described in the pretreatment for HAADF-STEM and STEM-EDX analyses.

ProQEXAFS[48] software was used to subtract the baseline of the pre-edge and normalize the postedge processing of all X-ray absorption spectra. EXAFS analysis was carried out using a Fourier transform on k^2-weighted EXAFS oscillations. The curve fitting of steady-state EXAFS spectra was conducted using the Artemis software of the Demeter program. The concurrent analysis of transient EXAFS with global constraints, MCR-ALS, and PSD analyses were done using custom Python scripts and open-source Python packages: pyMCR and xraylarch.

7. COMPUTATIONAL METHODS

We performed DFT calculations using plane-wave basis sets and the projector augmented-wave (PAW) method,[51] as implemented in the Vienna Ab Initio Simulation Package (VASP).[52] The plane-wave kinetic energy cutoff was set at 450 eV. The Methfessel-Paxton smearing scheme[53] was employed with a broadening value of 0.2 eV. All structures were optimized via ionic relaxation, with the total energy and forces converged to 10−5 and 0.02 eV/Å, respectively. Gas-phase H_2 was optimized in a 14 × 15 × 16 $Å^3$ cell at the Γ-point. Lattice constants of bulk face-centered cubic Au, Pd, and Pd_1Au_3 alloy were optimized according to the third-order Birch−Murnaghan equation of state,[54,55] using a 19 × 19 × 19 and 10 × 10 × 10 Monkhorst−Pack k-point grid[56] for the pure and alloy systems, respectively. Unless stated otherwise, we employed the alloy lattice constant for all Pd/Au(111) slab models to reflect the global concentration of Pd in the synthesized bimetallic nanoparticles. All slab models with 4, 5, and 6 layers were spaced by 12, 14, and 16 Å of vacuum, respectively, along the direction normal to the surface to avoid spurious interactions between adjacent unit cells. We fixed the bottommost layer at bulk positions to mimic bulk properties. The Brillouin zone was sampled using a Γ-centered 5 × 5 × 1, 4 × 4 × 1, 3 × 3 × 1, and 3 × 3 × 1 k-point grid for a 3 × 3, 4 × 4, 5 × 5, and 6 × 6 unit cell of the (111) facet, respectively.

We employed the generalized gradient approximation (GGA) Perdew−Burke−Ernzerhof (PBE) exchange−correlation functional, along with the dDsC dispersion correction[57−59] to account for van der Waals interactions. PBE-dDsC provided Au and Pd lattice constants of 4.14 and 3.93 Å, within <0.1 Å of the experimental benchmark of 4.08 and 3.88 Å, respectively.[60] The optimized lattice constant of the Pd_1Au_3 alloy was 4.09 Å, in good agreement with the experimental value of 4.03 Å expected from Vegard's law.[61]

■ ASSOCIATED CONTENT

Supporting Information

The Supporting Information is available free of charge at https://pubs.acs.org/doi/10.1021/jacs.5c00842.

MCR-ALS, EXAFS, and XANES analyses of time-resolved spectra, EXAFS analysis of steady-state spectra, computational details, Pd hydride stability assessment and formation process modeling, hydrogen diffusion pathways, and electron microscopy analysis (PDF)

■ AUTHOR INFORMATION

Corresponding Authors

Philippe Sautet − *Department of Chemical and Biomolecular Engineering and Department of Chemistry and Biochemistry, University of California, Los Angeles, Los Angeles, California 90095, United States;* orcid.org/0000-0002-8444-3348; Email: sautet@ucla.edu

Anatoly I. Frenkel − *Department of Materials Science and Chemical Engineering, Stony Brook University, Stony Brook, New York 11794, United States; Division of Chemistry, Brookhaven National Laboratory, Upton, New York 11973, United States;* orcid.org/0000-0002-5451-1207; Email: anatoly.frenkel@stonybrook.edu

Authors

Prahlad K. Routh − *Department of Materials Science and Chemical Engineering, Stony Brook University, Stony Brook, New York 11794, United States*

Xihan Liu − *Department of Chemical and Biomolecular Engineering, University of California, Los Angeles, Los Angeles, California 90095, United States*

Evgeniy Redekop − *Centre for Materials Science and Nanotechnology (SMN), Department of Chemistry, University of Oslo, N-0315 Oslo, Norway*

Jin Soo Lim − *Department of Chemical and Biomolecular Engineering, University of California, Los Angeles, Los Angeles, California 90095, United States*

Sebastian Prodinger − *Centre for Materials Science and Nanotechnology (SMN), Department of Chemistry, University of Oslo, N-0315 Oslo, Norway*

Jessi E. S. van der Hoeven − *Materials Chemistry and Catalysis, Debye Institute for Nanomaterials Science, Utrecht University, 3584 CG Utrecht, The Netherlands;* orcid.org/0000-0001-9832-289X

Joanna Aizenberg − *Harvard John A. Paulson School of Engineering and Applied Sciences and Department of Chemistry and Chemical Biology, Harvard University, Cambridge, Massachusetts 02138, United States;* orcid.org/0000-0002-2343-8705

Maarten Nachtegaal − *Center for Photon Science and Center for Energy and Environmental Sciences, PSI, CH-5232 Villigen, Switzerland; Department of Chemistry, ETH Zürich, CH-8093 Zürich, Switzerland;* orcid.org/0000-0003-1895-9626

Adam H. Clark − *Center for Photon Science, PSI, CH-5232 Villigen, Switzerland;* orcid.org/0000-0002-5478-9639

Complete contact information is available at: https://pubs.acs.org/10.1021/jacs.5c00842

Author Contributions

●P.K.R., X.L., and E.R. contributed equally to this work.

Notes

The authors declare no competing financial interest.

■ ACKNOWLEDGMENTS

This project was primarily supported by Integrated Mesoscale Architectures for Sustainable Catalysis (IMASC), an Energy Frontier Research Center funded by the US Department of Energy, Office of Science, Office of Basic Energy Sciences, Award No. DE-SC0012573. J.S.L. used the Cannon Cluster, FAS Division of Science, Research Computing Group at Harvard University; and the National Energy Research Scientific Computing Center (NERSC), a US Department of Energy Office of Science User Facility supported under Contract No. DE-AC02-05CH11231, through allocation m3275. X.L. used the HOFFMAN2 cluster at the UCLA Institute for Digital Research and Education (IDRE). E.R. and S.P. acknowledge the iCSI (industrial Catalysis Science and innovation) Centre for Research-Based Innovation, which receives financial support from the Research Council of Norway under contract no. 237922. The Swiss Light Source is acknowledged for the provision of beamtime at the SuperXAS beamline. JESvdH acknowledges funding from the NWO Veni project with project number VI.Veni.212.046, which is financed by the Dutch Research Council (NWO), and funding for access to the TFS Spectra300 at EM Utrecht from The Netherlands Electron Microscopy Infrastructure (NEMI), project number 184.034.014, part of the National Roadmap and financed by the Dutch Research Council.

■ REFERENCES

(1) Pyle, D. S.; Gray, E. M.; Webb, C. Hydrogen storage in carbon nanostructures via spillover. *Int. J. Hydrogen Energy* **2016**, *41* (42), 19098−19113.

(2) Dong, C.; Gao, Z.; Li, Y.; Peng, M.; Wang, M.; Xu, Y.; Li, C.; Xu, M.; Deng, Y.; Qin, X.; et al. Fully exposed palladium cluster catalysts enable hydrogen production from nitrogen heterocycles. *Nat. Catal.* **2022**, *5* (6), 485−493.

(3) Kaiser, S. K.; Van Der Hoeven, J. E.; Yan, G.; Lim, K. R. G.; Ngan, H. T.; Garg, S.; Karatok, M.; Aizenberg, M.; Aizenberg, J.; Sautet, P.; et al. Identifying the optimal Pd ensemble size in dilute PdAu alloy nanomaterials for benzaldehyde hydrogenation. *ACS Catal.* **2023**, *13* (18), 12092−12103.

(4) Zhao, X.; Chang, Y.; Chen, W.-J.; Wu, Q.; Pan, X.; Chen, K.; Weng, B. Recent Progress in Pd-Based Nanocatalysts for Selective Hydrogenation. *ACS Omega* **2022**, *7* (1), 17−31.

(5) Ball, M. R.; Rivera-Dones, K. R.; Gilcher, E. B.; Ausman, S. F.; Hullfish, C. W.; Lebrón, E. A.; Dumesic, J. A. AgPd and CuPd catalysts for selective hydrogenation of acetylene. *ACS Catal.* **2020**, *10* (15), 8567−8581.

(6) Pei, G. X.; Liu, X. Y.; Wang, A.; Lee, A. F.; Isaacs, M. A.; Li, L.; Pan, X.; Yang, X.; Wang, X.; Tai, Z.; et al. Ag alloyed Pd single-atom catalysts for efficient selective hydrogenation of acetylene to ethylene in excess ethylene. *ACS Catal.* **2015**, *5* (6), 3717−3725.

(7) Marcella, N.; Lim, J. S.; Plonka, A. M.; Yan, G.; Owen, C. J.; van der Hoeven, J. E. S.; Foucher, A. C.; Ngan, H. T.; Torrisi, S. B.; Marinkovic, N. S.; et al. Decoding reactive structures in dilute alloy catalysts. *Nat. Commun.* **2022**, *13* (1), 832.

(8) Silva, T. A.; Teixeira-Neto, É.; Borges, L. R.; Garcia, T. N.; Braga, A. H.; Rossi, L. M. From AuPd nanoparticle alloys towards core-shell motifs with enhanced alcohol oxidation activity. *ChemCatChem* **2023**, *15*, No. e202300180.

(9) Dimitratos, N.; Vilé, G.; Albonetti, S.; Cavani, F.; Fiorio, J.; López, N.; Rossi, L. M.; Wojcieszak, R. Strategies to improve hydrogen activation on gold catalysts. *Nature Reviews Chemistry* **2024**, *8* (3), 195−210.

(10) van der Hoeven, J. E. S.; Jelic, J.; Olthof, L. A.; Totarella, G.; van Dijk-Moes, R. J. A.; Krafft, J.-M.; Louis, C.; Studt, F.; van Blaaderen, A.; de Jongh, P. E. Unlocking synergy in bimetallic catalysts by core-shell design. *Nat. Mater.* **2021**, *20*, 1216−1220.

(11) Bugaev, A. L.; Guda, A. A.; Lomachenko, K. A.; Srabionyan, V. V.; Bugaev, L. A.; Soldatov, A. V.; Lamberti, C.; Dmitriev, V. P.; van Bokhoven, J. A. Temperature-and pressure-dependent hydrogen concentration in supported PdH x nanoparticles by Pd K-edge X-ray absorption spectroscopy. *J. Phys. Chem. C* **2014**, *118* (19), 10416−10423.

(12) Chase, Z. A.; Fulton, J. L.; Camaioni, D. M.; Mei, D.; Balasubramanian, M.; Pham, V.-T.; Zhao, C.; Weber, R. S.; Wang, Y.; Lercher, J. A. State of supported Pd during catalysis in water. *J. Phys. Chem. C* **2013**, *117* (34), 17603−17612.

(13) Haug, K.; Bürgi, T.; Trautman, T.; Ceyer, S. Distinctive reactivities of surface-bound H and bulk H for the catalytic hydrogenation of acetylene. *J. Am. Chem. Soc.* **1998**, *120* (34), 8885−8886.

(14) Teschner, D.; Borsodi, J.; Wootsch, A.; Révay, Z.; Havecker, M.; Knop-Gericke, A.; Jackson, S. D.; Schlögl, R. The roles of subsurface carbon and hydrogen in palladium-catalyzed alkyne hydrogenation. *Science* **2008**, *320* (5872), 86−89.

(15) Hong, J.; Bae, J.-H.; Jo, H.; Park, H.-Y.; Lee, S.; Hong, S. J.; Chun, H.; Cho, M. K.; Kim, J.; Kim, J.; et al. Metastable hexagonal close-packed palladium hydride in liquid cell TEM. *Nature* **2022**, *603* (7902), 631−636.

(16) Morkel, M.; Rupprechter, G.; Freund, H.-J. Finite size effects on supported Pd nanoparticles: Interaction of hydrogen with CO and C2H4. *Surf. Sci.* **2005**, *588* (1), L209−L219.
(17) Teschner, D.; Borsodi, J.; Kis, Z.; Szentmiklósi, L.; Révay, Z.; Knop-Gericke, A.; Schlögl, R.; Torres, D.; Sautet, P. Role of Hydrogen Species in Palladium-Catalyzed Alkyne Hydrogenation. *J. Phys. Chem. C* **2010**, *114* (5), 2293−2299.
(18) Lewis, A. E.; Kershner, D. C.; Paglieri, S. N.; Slepicka, M. J.; Way, J. D. Pd−Pt/YSZ composite membranes for hydrogen separation from synthetic water−gas shift streams. *J. Membr. Sci.* **2013**, *437*, 257−264.
(19) Omidifar, M.; Akbar Babaluo, A. Hydrogen flux improvement through palladium and its alloy membranes: Investigating influential parameters-A review. *Fuel* **2025**, *379*, No. 133038.
(20) Griessen, R.; Strohfeldt, N.; Giessen, H. Thermodynamics of the hybrid interaction of hydrogen with palladium nanoparticles. *Nat. Mater.* **2016**, *15* (3), 311−317.
(21) Baldi, A.; Narayan, T. C.; Koh, A. L.; Dionne, J. A. In situ detection of hydrogen-induced phase transitions in individual palladium nanocrystals. *Nat. Mater.* **2014**, *13*, 1143−1148.
(22) Pati, S.; Jat, R. A.; Mukerjee, S. K.; Parida, S. C. Hydrogen Isotope Effect on Thermodynamic and Kinetics of Hydrogen/Deuterium Absorption−Desorption in Pd0.77Ag0.10Cu0.13 Alloy. *J. Phys. Chem. C* **2015**, *119* (19), 10314−10320.
(23) Hosseini, M.; Barakat, T.; Cousin, R.; Aboukaïs, A.; Su, B.-L.; De Weireld, G.; Siffert, S. Catalytic performance of core−shell and alloy Pd−Au nanoparticles for total oxidation of VOC: The effect of metal deposition. *Applied Catalysis B: Environmental* **2012**, *111*, 218−224.
(24) Knecht, M. R.; Weir, M. G.; Frenkel, A. I.; Crooks, R. M. Structural rearrangement of bimetallic alloy PdAu nanoparticles within dendrimer templates to yield core/shell configurations. *Chemistry of materials* **2008**, *20* (3), 1019−1028.
(25) Kan, C.; Cai, W.; Li, C.; Zhang, L.; Hofmeister, H. Ultrasonic synthesis and optical properties of Au/Pd bimetallic nanoparticles in ethylene glycol. *J. Phys. D: Appl. Phys.* **2003**, *36* (13), 1609.
(26) Luneau, M.; Shirman, T.; Filie, A.; Timoshenko, J.; Chen, W.; Trimpalis, A.; Flytzani-Stephanopoulos, M.; Kaxiras, E.; Frenkel, A. I.; Aizenberg, J.; et al. Dilute Pd/Au alloy nanoparticles embedded in colloid-templated porous SiO2: stable Au-based oxidation catalysts. *Chem. Mater.* **2019**, *31* (15), 5759−5768.
(27) Merrill, N. A.; McKee, E. M.; Merino, K. C.; Drummy, L. F.; Lee, S.; Reinhart, B.; Ren, Y.; Frenkel, A. I.; Naik, R. R.; Bedford, N. M.; et al. Identifying the atomic-level effects of metal composition on the structure and catalytic activity of peptide-templated materials. *ACS Nano* **2015**, *9* (12), 11968−11979.
(28) Baber, A. E.; Tierney, H. L.; Sykes, E. C. H. Atomic-scale geometry and electronic structure of catalytically important Pd/Au alloys. *ACS Nano* **2010**, *4* (3), 1637−1645.
(29) Ricciardulli, T.; Gorthy, S.; Adams, J. S.; Thompson, C.; Karim, A. M.; Neurock, M.; Flaherty, D. W. Effect of Pd coordination and isolation on the catalytic reduction of O2 to H2O2 over PdAu bimetallic nanoparticles. *J. Am. Chem. Soc.* **2021**, *143* (14), 5445−5464.
(30) Qiao, S.; Shou, H.; Xu, W.; Cao, Y.; Zhou, Y.; Wang, Z.; Wu, X.; He, Q.; Song, L. Regulating and identifying the structures of PdAu alloys with splendid oxygen reduction activity for rechargeable zinc−air batteries. *Energy Environ. Sci.* **2023**, *16* (12), 5842−5851.
(31) Srinivas, S.; Vlachos, D. G. Tuning at the subnanometre scale. *Nature Catalysis* **2022**, *5* (6), 467−468.
(32) Routh, P. K.; Redekop, E.; Prodinger, S.; van der Hoeven, J. E.; Lim, K. R. G.; Aizenberg, J.; Nachtegaal, M.; Clark, A. H.; Frenkel, A. I. Restructuring dynamics of surface species in bimetallic nanoparticles probed by modulation excitation spectroscopy. *Nat. Commun.* **2024**, *15* (1), 6736.
(33) van der Hoeven, J. E. S.; Krämer, S.; Dussi, S.; Shirman, T.; Park, K.-C. K.; Rycroft, C. H.; Bell, D. C.; Friend, C. M.; Aizenberg, J. On the Origin of Sinter-Resistance and Catalyst Accessibility in Raspberry-Colloid-Templated Catalyst Design. *Adv. Funct. Mater.* **2021**, *31* (49), No. 2106876.
(34) Hoeven, J. E. S. V. D.; Shneidman, A. V.; Nicolas, N. J.; Aizenberg, J. Evaporation-Induced Self-Assembly of Metal Oxide Inverse Opals: From Synthesis to Applications. *Acc. Chem. Res.* **2022**, *55* (13), 1809−1820.
(35) Guan, E.; Foucher, A. C.; Marcella, N.; Shirman, T.; Luneau, M.; Head, A. R.; Verbart, D. M. A.; Aizenberg, J.; Friend, C. M.; Stacchiola, D.; et al. New Role of Pd Hydride as a Sensor of Surface Pd Distributions in Pd−Au Catalysts. *ChemCatChem.* **2020**, *12* (3), 717−721.
(36) Wang, J.; Wang, Q.; Jiang, X.; Liu, Z.; Yang, W.; Frenkel, A. I. Determination of Nanoparticle Size by Measuring the Metal−Metal Bond Length: The Case of Palladium Hydride. *J. Phys. Chem. C* **2015**, *119* (1), 854−861.
(37) Feenstra, R.; Griessen, R.; Groot, D. G. D. Hydrogen induced lattice expansion and effective H-H interaction in single phase PdHc. *Journal of Physics F: Metal Physics* **1986**, *16* (12), 1933.
(38) Fovanna, T.; Nachtegaal, M.; Clark, A. H.; Krocher, O.; Ferri, D. Preparation, quantification, and reaction of Pd hydrides on Pd/Al2O3 in liquid environment. *ACS Catal.* **2023**, *13* (5), 3323−3332.
(39) Doronkin, D. E.; Wang, S.; Sharapa, D. I.; Deschner, B. J.; Sheppard, T. L.; Zimina, A.; Studt, F.; Dittmeyer, R.; Behrens, S.; Grunwaldt, J.-D. Dynamic structural changes of supported Pd, PdSn, and PdIn nanoparticles during continuous flow high pressure direct H2O2 synthesis. *Catalysis Science & Technology* **2020**, *10* (14), 4726−4742.
(40) Urakawa, A.; Bürgi, T.; Baiker, A. Kinetic analysis using square-wave stimulation in modulation excitation spectroscopy: Mixing property of a flow-through PM-IRRAS cell. *Chem. Phys.* **2006**, *324* (2−3), 653−658.
(41) Chiarello, G. L.; Ferri, D. Modulated excitation extended X-ray absorption fine structure spectroscopy. *Phys. Chem. Chem. Phys.* **2015**, *17* (16), 10579−10591.
(42) Ferri, D.; Newton, M. A.; Nachtegaal, M. Modulation Excitation X-Ray Absorption Spectroscopy to Probe Surface Species on Heterogeneous Catalysts. *Top Catal* **2011**, *54* (16−18), 1070−1078.
(43) Marchionni, V.; Ferri, D.; Krocher, O.; Wokaun, A. Increasing the Sensitivity to Short-Lived Species in a Modulated Excitation Experiment. *Anal. Chem.* **2017**, *89* (11), 5801−5809.
(44) Bugaev, A. L.; Guda, A. A.; Lazzarini, A.; Lomachenko, K. A.; Groppo, E.; Pellegrini, R.; Piovano, A.; Emerich, H.; Soldatov, A. V.; Bugaev, L. A.; et al. In situ formation of hydrides and carbides in palladium catalyst: When XANES is better than EXAFS and XRD. *Catal. Today* **2017**, *283*, 119−126.
(45) Foucher, A. C.; Owen, C. J.; Shirman, T.; Aizenberg, J.; Kozinsky, B.; Stach, E. A. Atomic-Scale STEM Analysis Shows Structural Changes of Au−Pd Nanoparticles in Various Gaseous Environments. *J. Phys. Chem. C* **2022**, *126* (42), 18047−18056.
(46) Greeley, J.; Mavrikakis, M. Surface and subsurface hydrogen: adsorption properties on transition metals and near-surface alloys. *J. Phys. Chem. B* **2005**, *109* (8), 3460−3471.
(47) Kristinsdóttir, L.; Skúlason, E. A systematic DFT study of hydrogen diffusion on transition metal surfaces. *Surf. Sci.* **2012**, *606* (17−18), 1400−1404.
(48) Nazarov, R.; Hickel, T.; Neugebauer, J. Ab initio study of H-vacancy interactions in fcc metals: Implications for the formation of superabundant vacancies. *Phys. Rev. B* **2014**, *89* (14), No. 144108.
(49) Lee, J. D.; Miller, J. B.; Shneidman, A. V.; Sun, L.; Weaver, J. F.; Aizenberg, J.; Biener, J.; Boscoboinik, J. A.; Foucher, A. C.; Frenkel, A. I.; et al. Dilute Alloys Based on Au, Ag, or Cu for Efficient Catalysis: From Synthesis to Active Sites. *Chem. Rev.* **2022**, *122* (9), 8758−8808.
(50) Müller, O.; Nachtegaal, M.; Just, J.; Lützenkirchen-Hecht, D.; Frahm, R. Quick-EXAFS setup at the SuperXAS beamline for in situ X-ray absorption spectroscopy with 10 ms time resolution. *Journal of Synchrotron Radiation* **2016**, *23* (1), 260−266.

(51) Blöchl, P. E. Projector augmented-wave method. *Phys. Rev. B* **1994**, *50* (24), 17953.
(52) Kresse, G. Ab initio molecular dynamics for liquid metals. *J. Non-Cryst. Solids* **1995**, *192*, 222−229.
(53) Methfessel, M.; Paxton, A. High-precision sampling for Brillouin-zone integration in metals. *Phys. Rev. B* **1989**, *40* (6), 3616−3621.
(54) Birch, F. Finite elastic strain of cubic crystals. *Phys. Rev.* **1947**, *71* (11), 809−824.
(55) Murnaghan, F. D. The compressibility of media under extreme pressures. *Proc. Natl. Acad. Sci. U. S. A.* **1944**, *30* (9), 244−247.
(56) Monkhorst, H. J.; Pack, J. D. Special points for Brillouin-zone integrations. *Phys. Rev. B* **1976**, *13* (12), 5188−5192.
(57) Gautier, S.; Steinmann, S. N.; Michel, C.; Fleurat-Lessard, P.; Sautet, P. Molecular adsorption at Pt (111). How accurate are DFT functionals? *Phys. Chem. Chem. Phys.* **2015**, *17* (43), 28921−28930.
(58) Steinmann, S. N.; Corminboeuf, C. A generalized-gradient approximation exchange hole model for dispersion coefficients. *J. Chem. Phys.* **2011**, *134* (4), No. 044117.
(59) Steinmann, S. N.; Corminboeuf, C. Comprehensive benchmarking of a density-dependent dispersion correction. *J. Chem. Theory Comput.* **2011**, *7* (11), 3567−3577.
(60) Csonka, G. I.; Perdew, J. P.; Ruzsinszky, A.; Philipsen, P. H.; Lebègue, S.; Paier, J.; Vydrov, O. A.; Ángyán, J. G. Assessing the performance of recent density functionals for bulk solids. *Phys. Rev. B* **2009**, *79* (15), No. 155107.
(61) Ashcroft, N.; Denton, A. Vegard's law. *Phys. Rev. A* **1991**, *43* (6), 3161−3164.

https://doi.org/10.1021/jacs.5c00842
J. Am. Chem. Soc. 2025, 147, 11378−11389